

LASER INTERFEROMETER GRAVITATIONAL WAVE OBSERVATORY
- LIGO -
CALIFORNIA INSTITUTE OF TECHNOLOGY
MASSACHUSETTS INSTITUTE OF TECHNOLOGY

LIGO-P010015-02 D

24 Sept 2001

Lock acquisition of a gravitational wave interferometer

M. Evans, N. Mavalvala, P. Fritschel, R. Bork, B. Bhawal, R. Gustafson, W. Kells, M. Landry, D. Sigg, R. Weiss, S. Whitcomb, H. Yamamoto

Distribution of this draft:

LIGO Laboratory

This is an internal working note
of the LIGO Project.

California Institute of Technology
LIGO Project - MS 51-33
Pasadena CA 91125
Phone (818) 395-2129
Fax (818) 304-9834
E-mail: info@ligo.caltech.edu

Massachusetts Institute of Technology
LIGO Project - NW17-161
Cambridge, MA 01239
Phone (617) 253-4824
Fax (617) 253-7014
E-mail: info@ligo.mit.edu

WWW: <http://www.ligo.caltech.edu/>

Lock acquisition of a gravitational wave interferometer

M. Evans, N. Mavalvala, P. Fritschel, R. Bork, B. Bhawal, R. Gustafson, W. Kells,

M. Landry, D. Sigg, R. Weiss, S. Whitcomb, H. Yamamoto

LIGO Hanford Observatory, P.O. Box 1970 S9-02, Richland, WA 99352

Interferometric gravitational wave detectors, such as the LIGO detectors currently under construction, are based on km-scale Michelson interferometers, with the sensitivity enhanced by adding multiple coupled optical resonators. Reducing the relative optic motions to bring the system to the resonant operating point is a significant challenge. We present a new approach to lock acquisition—used to successfully lock a LIGO interferometer—whereby the sensor transformation matrix is dynamically calculated to sequentially bring the cavities into resonance.

OCIS codes: 120.3180, 140.4780, 120.2230

Long baseline interferometric gravitational wave detectors use variants of the Michelson interferometer to convert gravitational-wave strain into optical phase difference in an efficient manner¹. Resonant optical cavities are typically used in the arms to build up the interaction time of the light beams with the gravitational wave, increasing the phase difference by a factor proportional to the cavity finesse; the LIGO interferometers, e.g., contain a 2- or 4-km-long cavity in each arm of the Michelson. A partially transmitting mirror at the input couples these arm cavities to form a third resonant cavity—the power recycling cavity—which builds up the power incident on the beam splitter. To achieve the full sensitivity of the instrument, the resonance condition of each cavity and the destructive interference condition at the antisymmetric port of the interferometer must be met to within tolerances of $10^{-10} - 10^{-13}$ m, against a continuous background of ground motion driving the optic supports. To reduce these disturbances, all detectors implement an isolation system from which the mirrors are suspended as pendula; in LIGO this system provides high isolation for frequencies above ~ 40 Hz, though minimal isolation below a few Hertz.

The LIGO control system has two distinct functions: to *maintain* the interferometer at the operating point, using linear time-invariant feedback from a phase modulation/demodulation system which provides linear error signals for small deviations (of order 1 nm) from the operating point^{2,3}, and to *acquire lock* by initially stabilizing the relative optic positions to establish the resonance conditions and bring them within the linear regions of the error signals. Previous prototype interferometers (lengths up to tens of meters) have approached lock acquisition in various ways: some as rudimentary as the ‘wait for it to lock’ approach—where random ground motion coincidentally positions the mirrors near resonance; more deliberate methods include a relative velocity damping technique used for a single arm cavity.⁴ Here we present a new approach to lock acquisition of a power-recycled, Fabry-Perot Michelson interferometer, used to lock the

LIGO Hanford Observatory's 2km interferometer. Using a time-domain simulation of the interferometer, an algorithm has been developed that sequentially brings into lock the various degrees of freedom, using measurable optical signals to estimate the time-evolving sensing matrix and applying feedback forces to reduce the mirrors' relative velocities.

The acquisition strategy uses the sensors designed for linear control of the resonant interferometer's four longitudinal degrees of freedom (Fig. 1). A combination of Pound-Drever-Hall reflection sensing and the Schnupp asymmetry scheme is used to generate error signals for small deviations from the operating point. Radio-frequency (rf) phase modulation sidebands are imposed on the input light, and the outputs of photodetectors receiving light from three ports are demodulated in both phases at the rf frequency to yield four linearly independent signals. These signals naturally separate into common and differential mode motions: common and differential arm lengths, L_+ and L_- , recycling cavity length, l_+ , and Michelson length, l_- . The nominal lengths are chosen so that at the operating point the first-order phase modulation sidebands: *i*) resonate in the recycling cavity, *ii*) are nearly antiresonant in the arm cavities, *iii*) transmit efficiently to the antisymmetric port.

Initially the suspended optics are damped within their local reference frame; ground motion, and the equivalent effect of input light frequency fluctuations cause the four (real or apparent) lengths to fluctuate by $\sim 0.1\text{--}1\ \mu\text{m}$ -rms over time scales of $\sim 0.5\text{--}10$ seconds. The probability of all four degrees of freedom being simultaneously within the $\sim 1\ \text{nm}$ linear region of the resonance points is thus extremely small, and a sequential locking approach must be taken, whereby degrees of freedom are captured in sequence as follows (see Fig. 2a). First, the recycling cavity and Michelson lengths are brought to the point where the former is resonant for the rf sidebands, and the latter is at a carrier dark fringe. In this state—called 'state 2' since two degrees of freedom are

locked—the carrier is antiresonant in the recycling cavity, as it does not yet experience the π phase shift in reflecting from resonant, over-coupled arm cavities. Next, one of the arm cavities is captured at a carrier resonance; in this ‘state 3’, the l_+ and l_- lengths are unchanged, so the carrier interferes destructively at the symmetric side of the beam splitter and there is still no significant buildup of the carrier in the recycling cavity. Finally, a carrier resonance of the other arm cavity is captured and the full power buildup is achieved in ‘state 4’.

Recovering error signals for each degree of freedom during the acquisition sequence is more of a challenge. The signal separation is generally not clean since the fields may not be balanced in the arms and the gain hierarchy may not be established; the optical gain matrix \mathbf{G} relating the degrees of freedom \mathcal{D} to the output signals ($\mathcal{O} = \mathbf{G}\mathcal{D}$) changes throughout acquisition. Our approach capitalizes on the fact that in the LIGO control system, the interferometer signals and the control signals are connected with a real-time digital control system capable of significant computation. The basic idea is to estimate the dominant elements of \mathbf{G} , continually update the estimation using measured power levels in the interferometer, and use it to dynamically construct a sensor transformation matrix \mathbf{M} to form the length error signals from the sensor signals: $\mathcal{D} = \mathbf{M}\mathcal{O}$.

The elements of \mathbf{G} are estimated using a generalization of the demodulation signals given in reference 3. They follow the general form:

$$G_{ij} = g_{ij} \sum A_{\text{LO}} A_{\text{res}} \gamma_{\text{sig}}, \quad (1)$$

relating the i th degree of freedom to the j th detection port. Each signal is the product of a local oscillator field A_{LO} , a resonant field A_{res} from which signal sidebands are generated, and a factor γ_{sig} representing the optical gain of the signal sidebands; the summation sign reflects that more than one local oscillator or resonant field may contribute to a signal. The scaling factors g contain

the fixed opto-electronic gain of the sensing hardware (reflectivities of beam sampling optics, photodetector gain, etc.). The essential elements of \mathbf{G} , given in Table 1, allow us to construct robust error signals for all degrees of freedom throughout the acquisition path, with one exception described below. We note that by scaling the demodulation signals by the field amplitudes, the effects of alignment fluctuations on the power buildup in the interferometer are accounted for.

In state 2, both degrees of freedom use the carrier for the local oscillator field; we use the reflection port demodulation signals since there is very little carrier in the recycling cavity, and the 2×2 matrix \mathbf{M} is diagonal: $M_{Q_{\text{ref}}, l_-} = G_{l_-, Q_{\text{ref}}}^{-1}$; $M_{I_{\text{ref}}, l_+} = G_{l_+, I_{\text{ref}}}^{-1}$. The l_- signal continues to be fed from Q_{ref} until state 4. In state 3, the arm cavity signal appears strongly at the antisymmetric port, but is also present in I_{ref} , along with l_+ . We thus invert the 2×2 matrix relating $\{I_{\text{ref}}, Q_{\text{as}}\}$ to $\{l_+, L_+\}$. Entering state 4, another demodulation signal, I_{rec} , must be added to sense the last degree of freedom. Three of the four degrees of freedom are strongly mixed at this point: with unbalanced power levels in the arms, L_{\pm} are mixed at all detection ports, and l_+ now also appears in the I_{rec} signal. We thus invert the 3×3 matrix relating $\{I_{\text{ref}}, I_{\text{rec}}, Q_{\text{as}}\}$ to $\{l_+, L_+, L_-\}$.

The resulting matrix \mathbf{M} produces robust error signals for the four degrees of freedom with one significant caveat: at some point as the power builds up in the arms, the I_{rec} and I_{ref} signals become degenerate, making l_+ and L_+ inseparable. This happens when $A_{\text{Srec}}/A_{\text{Sref}} = A_{\text{Crec}}/(A_{\text{Cref}} - A_{\text{S2ref}})$, a point which is almost inevitably crossed: the carrier recycling gain ($\propto A_{\text{Crec}}$) increases from less than unity in state 3 to some value greater than the sideband recycling gain when full power buildup is reached in state 4; at the same time the carrier reflectivity ($\propto A_{\text{Cref}}$) decreases from near unity to some small value, typically less than the sideband reflectivity.

When the determinant of the 3×3 optical gain matrix becomes small, it is not possible to derive

independent control signals for l_+ and L_+ . Since L_+ fluctuates more than l_+ and the system is less tolerant to L_+ deviation from resonance, we control L_+ and leave l_+ uncontrolled while the determinant is below some threshold. In this interval control signals for L_+ and L_- are derived from I_{ref} and Q_{as} by inverting the 2×2 matrix. As carrier buildup increases and the determinant again exceeds its threshold, the calculation returns to the 3×3 matrix.

Given expressions for the optical gain elements and a strategy for forming robust error signals, it remains to connect the parameters in the optical gain expressions to measurable quantities. There are seven field amplitudes and three signal gains to infer. They are all estimated using three direct power measurements and one additional demodulated rf signal. The power measurements are those of the light transmitted by each arm cavity and the reflected light. The REC signal – which produces I_{rec} and Q_{rec} – is also demodulated at twice the modulation frequency; this $2f_m$ demodulation signal is proportional to the recycling cavity sideband power and is used to estimate A_{Srec} . Measurements are made in states 2 and 3 (with unused end mirrors misaligned) to calibrate the signals, and to determine the scaling factors g .

This scheme of forming error signals is coupled with a strategy for applying feedback control forces to the suspended optics. The output matrix is straightforward: the L_+ and L_- signals are sent to both end test masses, driven in-phase or in anti-phase, respectively; l_+ is sent to the recycling mirror, and l_- to the beamsplitter and recycling mirror. Digital filtering is applied to each error signal to form stable feedback loops. As power builds up in state 4, the pole in the optical response to L_+ moves from that of the single arm cavity to the coupled-cavity pole frequency (a few Hz)³; the L_+ loop remains conditionally stable during this process, picking up additional low frequency gain.

We can now review the complete lock acquisition path, starting from the uncontrolled, non-res-

onant state. The approach of state 2 is indicated by the $2 \cdot f_m$ signal crossing a threshold (typically 30% of its maximum level); the sign of this signal distinguishes the desired rf sideband resonance from a carrier resonance. At this point, the l_+ and l_- error signals are calculated from I_{ref} and Q_{ref} . State 3 is approached when one of the arm cavities nears a carrier resonance, indicated by its transmission detector crossing a threshold (typically 10% of the state 3 level). This triggers the calculation of the 2x2 input matrix, producing a L_+ control signal. State 4 is entered when both arm cavity transmission detectors cross threshold, triggering the 3x3 input matrix calculation and activating the L_- control signal. The (normalized) determinant of this matrix is continuously calculated, and when its magnitude falls below a threshold value (typically 0.1), the (L_+, l_+) error signal separation becomes poor, and the l_+ control signal is turned off. Control of l_+ resumes when the determinant exceeds its threshold. Finally, the l_- error signal is switched from Q_{ref} to Q_{rec} when the arm power exceeds $\sim 10\times$ the state 3 level since the latter becomes more robust—the reflected signal scales with the reflected carrier field, which becomes small and possibly goes through zero. Note that the control signal for a given degree of freedom is produced only when the state containing it is triggered; input matrix coefficients for an error signal are otherwise zero.

A typical lock acquisition event is shown in Fig. 2. The channel sampling and calculation rate is 16,384/sec. The digital filtering consists of a real zero at 10 Hz applied to all four error signals to compensate for the pendulum response, and an additional real zero at ~ 100 Hz applied to the L_+ and L_- signals to compensate the arm cavity pole; unity gain frequencies are ~ 150 Hz for the L loops, and ~ 30 Hz for the l loops. The filtering is rolled off with multiple poles above 1 kHz. The maximum peak force that can be applied to each mirror is approximately 8 mN, with a bandwidth of ~ 1 kHz.

The system acquires lock on average within 1–2 minutes. This is in the presence of average rel-

ative velocities of 0.2-0.5 $\mu\text{m}/\text{sec}$ for l , and 0.5-1 $\mu\text{m}/\text{sec}$ for L . If an arm cavity passes through an rf sideband resonance in state 2 or 3, the (l_+, l_-) error signals become contaminated, and the lock is typically broken, but state 2 is quickly recovered.

In summary, we have implemented an acquisition sequence to lock a LIGO interferometer, achieving a power recycling gain of up to 25. The dynamically calculated sensor transformation matrix does not rely on a gain hierarchy for proper signal separation, and deals successfully with the optical gain changes, most notably the singularity inherent in the system. The expected recycling gain of 30-50 should be achieved when the full angular alignment system is activated.

We thank our LIGO colleagues for their essential contributions in building the instruments. This work is supported by the National Science Foundation under Cooperative Agreement PHY-9210038. N. Mavalvala, R. Bork, B. Bhawal, W. Kells, S. Whitcomb, and H. Yamamoto are at the LIGO Lab, Caltech. P. Fritschel and R. Weiss are at the LIGO Lab at the Massachusetts Institute of Technology, Cambridge, MA; D. Gustafson is at the Department of Physics, University of Michigan. M. Evans' email address is mevans@ligo.caltech.edu.

References

1. B. C. Barish and R. Weiss, *Physics Today*, vol. **52**, no. **10**, 44 (1999).
2. M. W. Regehr, F. J. Raab, and S. E. Whitcomb, *Opt. Lett.* **20**, 1507 (1995).
3. P. Fritschel, M. Zucker, R. Bork, N. Mavalvala, D. Ouimette, G. González, H. Rong, and D. Sigg, to be published in *Applied Optics*.
4. J. Camp, L. Sievers, R. Bork, and J. Heefner, *Opt. Lett.* **20**, 2463 (1995).

Figure Captions.

Fig. 1. A power-recycled interferometer with detection ports shown. The REC and REF beams are shown schematically; in practice REC comes off the anti-reflection coated surface of the beam splitter or a cavity input mirror, and REF is separated from the input beam with a Faraday isolator. The power is detected on each detector; signals at the rf modulation frequency are detected at REF, REC and AS, using in- and quadrature-phase demodulation to generate length error signals (I_{ref} and Q_{ref} , e.g.). The signal at twice the modulation frequency is detected at REC.

Fig. 2. Top: Acquisition states of the interferometer. The rf sidebands (blue) resonate in the power recycling cavity only, while the carrier (red) resonates everywhere. Middle: Power levels during acquisition (\log_{10} vertical scale), normalized to the input sideband power (blue curve) and to the resonant arm power if there were no recycling mirror (green and red curves); horizontal bars indicate the corresponding states. Bottom: L_+ and l_+ control signals and the normalized determinant of the sensing matrix. During the state 3→4 transition the determinant goes through zero and the l_+ control signal is turned off for ~15 msec.

Tables.

Table 1: Elements of the optical gain matrix G .^a

<i>dof</i>	<i>Demodulation output</i>				
	I_{ref}	Q_{ref}	I_{rec}	Q_{rec}	Q_{as}
l_-		$(A_{C\text{ref}} + A_{S2\text{ref}}) \cdot A_{S\text{rec}} \gamma_{\text{prm}}$		$A_{C\text{ref}} A_{S\text{rec}} \gamma_{\text{prm}}$	
l_+	$(A_{C\text{ref}} - A_{S2\text{ref}}) \cdot A_{S\text{rec}} \gamma_{\text{prm}}$		$A_{C\text{rec}} A_{S\text{rec}} \gamma_{\text{prm}}$		
L_-	$A_{S\text{ref}} A_{C-}$		$A_{S\text{rec}} A_{C-}$		$A_{S\text{as}} A_{C+}$
L_+	$A_{S\text{ref}} A_{C+}$		$A_{S\text{rec}} A_{C+}$		$A_{S\text{as}} A_{C-}$

a. In terms of the field amplitudes for the carrier (A_C) and first and second order rf sidebands (A_S and A_{2S} respectively) at different points in the interferometer.

$A_{C\pm} = \gamma_1 A_1 \pm \gamma_2 A_2$, where (A_1, A_2) are the carrier field amplitudes in the arm cavities.

The γ 's are optical gain factors for the signal sidebands generated in the arms (γ_1, γ_2) and in the power recycled Michelson (γ_{prm}).

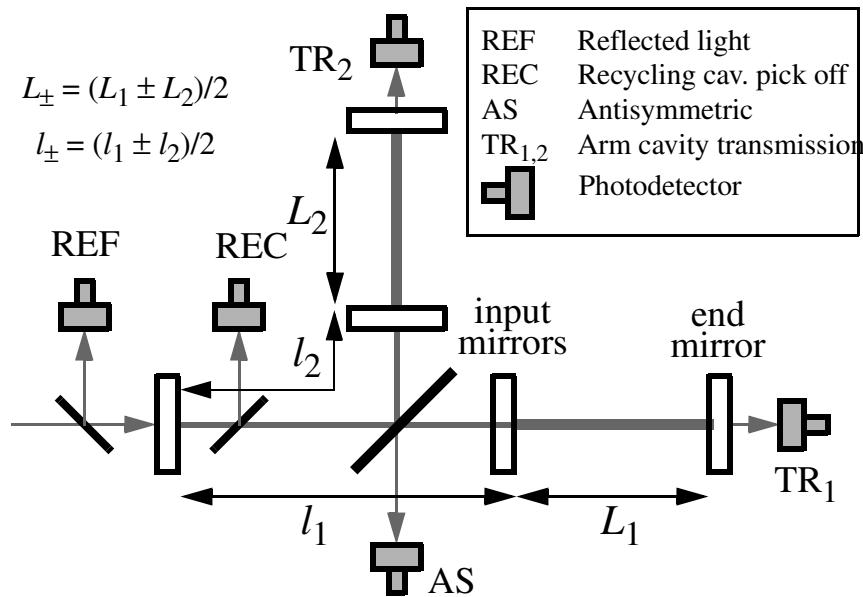


Figure 1. A power-recycled interferometer with detection ports shown. The REC and REF beams are shown schematically; in practice REC comes off the anti-reflection coated surface of the beam splitter or a cavity input mirror, and REF is separated from the input beam with a Faraday isolator. The power is detected on each detector; signals at the rf modulation frequency are detected at REF, REC and AS, using in- and quadrature-phase demodulation to generate length error signals (I_{ref} and Q_{ref} , e.g.). The signal at twice the modulation frequency is detected at REC.

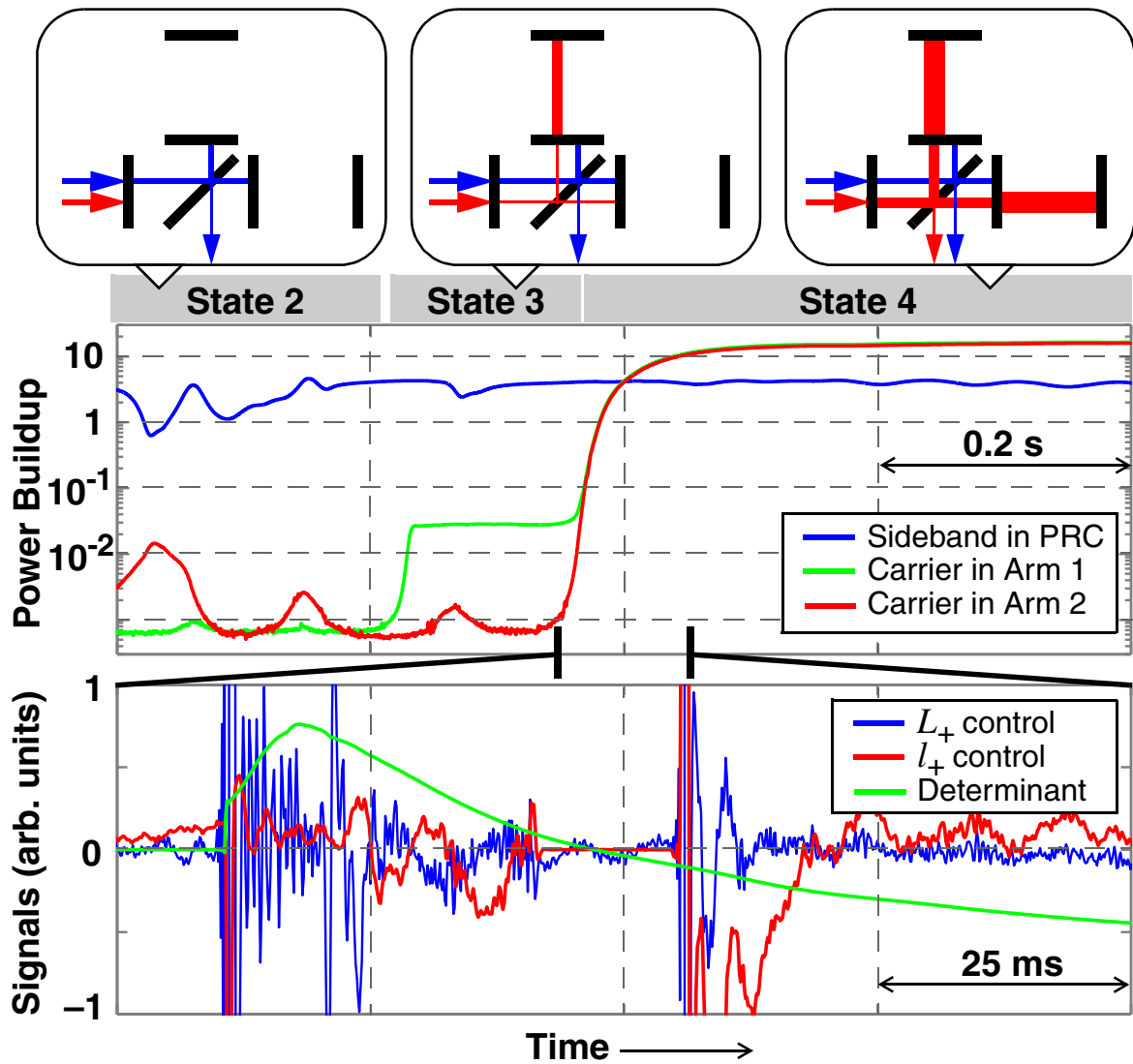


Figure 2. Top: Acquisition states of the interferometer. The rf sidebands (blue) resonate in the power recycling cavity only, while the carrier (red) resonates everywhere. Middle: Power levels during acquisition (\log_{10} vertical scale), normalized to the input sideband power (blue curve) and to the resonant arm power if there were no recycling mirror (green and red curves); horizontal bars indicate the corresponding states. Bottom: L_+ and l_+ control signals and the normalized determinant of the sensing matrix. During the state 3→4 transition the determinant goes through zero and the l_+ control signal is turned off for ~15 msec